PHYSICAL REVIEW FLUIDS **2**, 104502 (2017)

Scalar mixtures in porous media

Mihkel Kree[1,2,*] and Emmanuel Villermaux[2,3,†]
[1]*Institute of Cybernetics, Tallinn University of Technology, 12618 Tallinn, Estonia*
[2]*Aix Marseille Université, CNRS, Centrale Marseille, IRPHE UMR 7342, 13384 Marseille, France*
[3]*Institut Universitaire de France, 75005 Paris, France*
(Received 5 July 2017; published 23 October 2017)

Using a technique allowing for *in situ* measurements of concentrations fields, the evolution of scalar mixtures flowing within a porous medium made of a three-dimensional random stack of solid spheres, is addressed. Two distinct fluorescent dyes are injected from separate sources. Their evolution as they disperse and mix through the medium is directly observed and quantified, which is made possible by matching the refractive indices of the spheres and the flowing interstitial liquid. We decipher the nature of the interaction rule between the scalar sources, explaining the phenomenon that alters the concentration distribution of the overall mixture as it decays toward uniformity. Any residual correlation of the initially merged sources is progressively hidden, leading to an effective fully random interaction rule of the two distinct subfields.

DOI: 10.1103/PhysRevFluids.2.104502

I. INTRODUCTION

Mixing—the operation by which molecular diffusion and substrate deformation cooperate—is often discussed in the context of turbulent, or chaotic flows. However, effective mixing, namely the enhancement of molecular dissipation, may not solely be achieved by time-dependent motions. Mixing results from the stretching and folding of material surfaces in flows, leading to reinforced scalar concentration gradients which are then easily smeared by molecular diffusion. This may also occur in stationary laminar situations, provided the flow develops high strain rates, as those due to the no-slip boundary condition at solid surfaces like in a porous medium [1–3] or in other wall-bounded complicated geometries [4–6]. This type of flow, confined by solid surfaces in tortuous geometries, is widely encountered in nature such as in porous soils and fractured rocks [7], as well as in a variety of industrial apparatus and reactors [8,9].

A lot of attention has been devoted to measuring and describing the impact of an heterogeneous assembly of interconnected channels (pores) on the dispersion properties of a flow passing though it [10–12], and to understanding the origin of the possible anomalous, i.e., non-Gaussian, character of the resulting dispersion law [13–15]. However, experimental evidence of the microscopic structure of the scalar field, concentration content, and detailed mixing processes at the pore size are scarce for obvious reasons: Unless resorting to alternate diagnostics [16], confinement impedes three-dimensional direct imaging of the inside flow.

Using a technique allowing for the *in situ* visualization of concentrations fields in index-matched porous media [17], we provide here the first detailed measurements of the dynamics of a scalar mixture evolving in a porous medium. We quantify the topology of its concentration field and its concentration distribution, and decipher the interaction rule between distinct subparts of the mixture as it decays toward homogeneity.

*mihkel.kree@gmail.com
†emmanuel.villermaux@univ-amu.fr

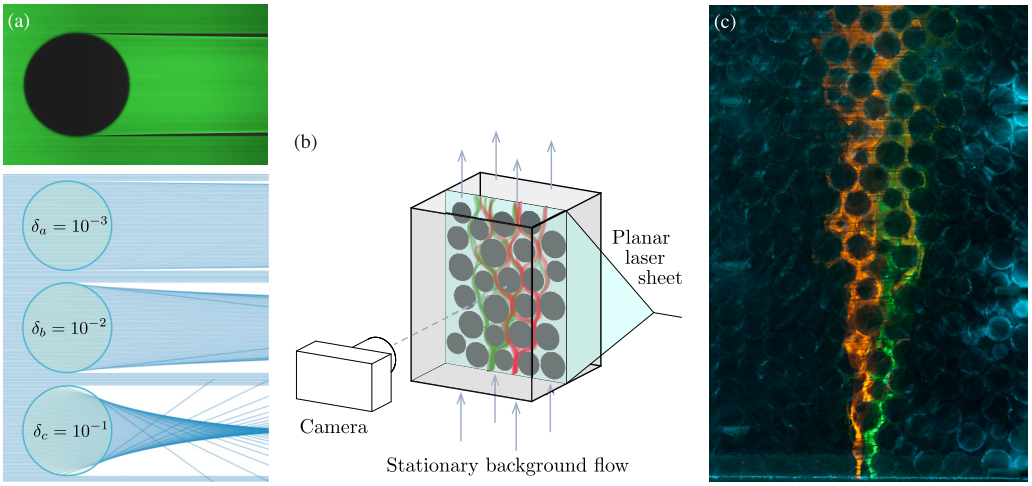

FIG. 1. (a) A bead, made of polyacrylamide hydrogel, placed in fluorescent water. Green regions mark the propagation of vertical planar laser sheet directed from left to right. Three sketches: Simple geometrical optical ray tracing illustrates the emergence of shadows and caustics from the top and bottom regions of the sphere due to slight relative mismatch $\delta = (n_b - n_w)/n_w$ of the refractive indices. (b) A sketch of the experimental setup: The direct imaging of the concentration fields inside the transparent porous medium is made possible by the fluorescence of the injected dyes at the plane of the laser sheet. (c) A raw, unfiltered snapshot of the tank filled with beads, cut by a planar laser sheet, showing how the two plumes of dyes are injected, disperse, mix, and interfere. The mean flow is from bottom to top.

II. SETUP AND METHODS

A. A near-transparent porous medium

A synthetic porous medium is formed by placing a three-dimensional random stack of solid spheres (beads) into a transparent tank through which flows an upward-directed stationary water stream. The porous medium is made transparent by matching the refractive indices of the beads with that of the water. The roughly monodispersed $d = 16\,\text{mm}$ in diameter "water beads" are made of a superabsorbent polymer (polyacrylamide hydrogel [18]) that can absorb a vast amount of water compared to its initial volume. This results in a close match of the refractive indices: The relative mismatch of the refractive indices n_b of the water-inflated beads and n_w of pure water is of the order of $(n_b - n_w)/n_w \approx 10^{-3}$. This estimate is based on the widths of the dark horizontal bands behind the extremal points of the spheres in the parallel light beam [Fig. 1(a)] and comparing them to the caustics calculated from geometrical optics of refraction. Other more elaborate index-matching methods are, however, even more precise [19].

The stack of spheres is placed into a vertical tank [see the sketch of the experimental setup in Fig. 1(b)]. The horizontal cross section of the tank is a square of side length $L = 12.5\,d$, and the height of the stack exceeds several side lengths. The porosity (void fraction) of this random close packing is $\phi \approx 0.3$. The upward flow of water is entering the tank from the bottom through a fine-mesh sintered bronze particle plate to ensure uniform flow distribution across the whole cross section, and the overflow is collected at the top of the tank. The flow rate of the mean uniform background flow rate is fixed to $R = 94\ \text{cm}^3\ \text{s}^{-1}$, corresponding to a mean interstitial velocity $u = R/\phi L^2 = 7.8\ \text{mm}\ \text{s}^{-1}$, giving the beads a Reynolds number of $ud/\nu = 125$ and a Péclet number $ud/D \approx 10^5$ with $D = 10^{-9}\ \text{m}^2\ \text{s}^{-1}$ being the order of magnitude of the molecular diffusion coefficient of fluorescein. Although responsible for the evolution of the concentration content of the mixture, molecular diffusion is thus not the rate-limiting step of the process in this high-Pé clet-number flow.

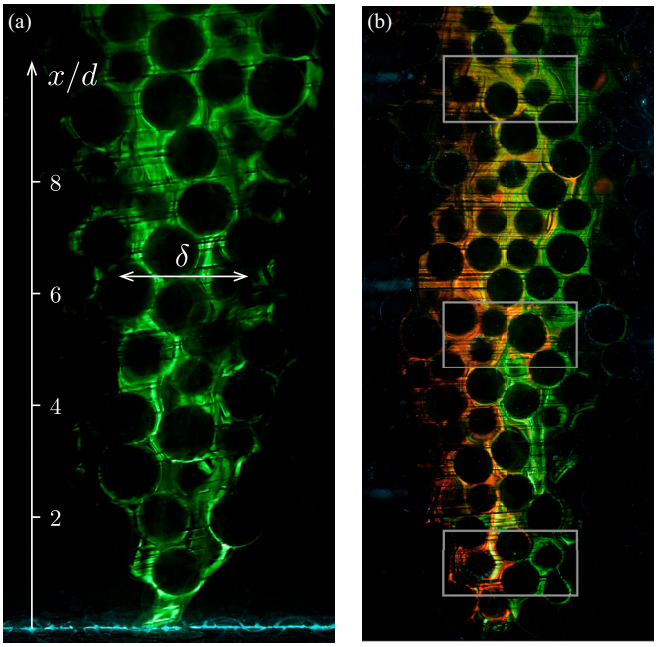

FIG. 2. Direct visualization of the concentration fields of the injected dyes inside the transparent porous medium. The stationary water flow is directed upward, and the planar laser sheet exciting the fluorescent emission of the dyes is directed from right to left. (a) Single dye injected at the bottom of the tank. (b) Two distinct dyes are injected side by side. The three rectangles indicate regions used for calculating the two-dimensional joint distributions of the two colors shown in Fig. 4.

B. Imaging

Two distinct fluorescent dyes, namely fluorescein (green) and rhodamine (red), are injected at the bottom of the tank from two small tubes of diameter $s_0 = 2\,\mathrm{mm} = d/8$, separated by a distance of the order of the bead diameter d. The dyes are injected at speeds roughly matching the mean velocity of the local interstitial flow. The fluorescence of these dyes is excited by a multimode argon-ion laser planar laser sheet aimed in the vertical plane and containing the injection tubes at the center of the tank. The 488-nm line of the laser is mainly absorbed by fluorescein, while the fluorescence of rhodamine is mainly excited by the 514-nm line. The fluorescence from both fields is recorded using a polarizing filter to get rid of the incident laser light reflections on the beads. Proper calibration and normalization by the injection concentrations give access to planar cuts of the concentration fields of both dyes, $C_1(x,y)$ for fluorescein and $C_2(x,y)$ for rhodamine inside the medium, where $\{x,y\}$ refers to the coordinates in the (discretized in 2400×3600 pixels) visualization plane [Fig. 1(b)]. The spatial resolution of the images is $100\,\mu$m per pixel.

The flow rates have been chosen sufficiently low so that the flow pattern and the concentration fields remain strictly stationary. Therefore, the wealth of information analyzed here is obtained from the analysis of single images as those shown in Fig. 2 solely.

We will first analyze the evolution of a mixture in a plume obtained by injecting a single dye only [fluorescein; see Fig. 2(a)] in the two injection tubes, whose concentration we call C. This allows us to extract the transverse dispersion properties in the porous medium as well as the downstream evolution of the concentration distributions $P(C)$. Then, in the spirit of an earlier study [20], we switch dye in one of the injection tubes in order to obtain a plume composed of two distinct colors initially, which allows us to describe the emergence and the nature of the interaction of the two fields based on the measured joint concentration distributions $Q(C_1,C_2)$. The downstream evolution of the

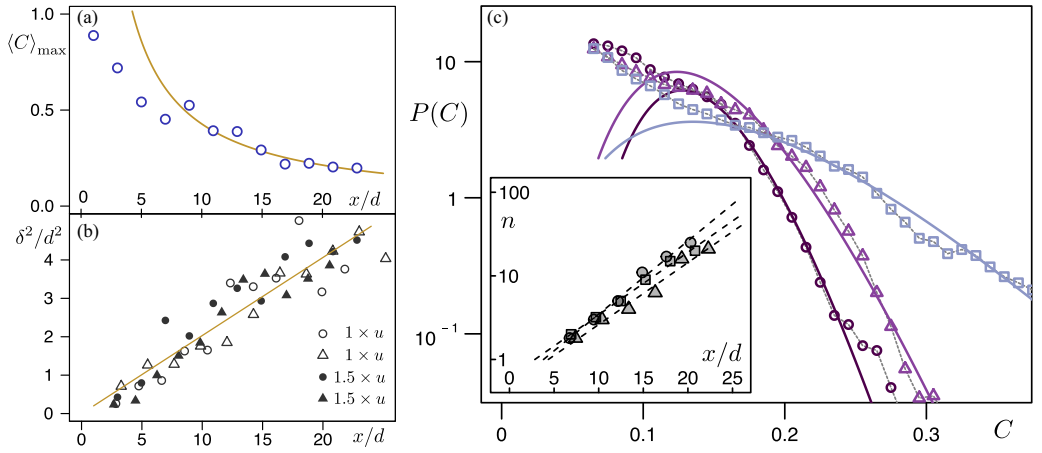

FIG. 3. (a) The concentration decays with distance $\langle C\rangle \sim x^{-1}$ (solid line) as suggested by Eq. (14). Note that it is difficult to measure the true average concentration $\langle C\rangle$ because the ever-increasing spacial domain needs to be properly taken into account in calculating the averages. Instead, we have plotted the average of top 1% of the concentration content in observation windows of fixed width, denoted by $\langle C\rangle_{\max}$, at various distances for a certain realization of the flow. (b) The variance $\delta^2(x)$ of the spreading plume of dye increases linearly with downstream distance x in accordance with Eq. (1). The data points correspond to two flow velocities, u and $1.5\,u$. (c) The lines with open markers indicate three concentration C (normalized by the injection concentration) distributions $P(C)$ at various downstream locations $x/d = 12$ (open squares), $x/d = 15$ (open triangles), and $x/d = 18$ (open circles) measured from an image such as the one shown on Fig. 2(a). The tails of these distributions are well fitted to weighted Γ distributions $\Gamma_n(C)$ (solid lines) of various shape parameters: $n = 5$, $n = 11$, $n = 17$ (in the order of increasing distance x). Inset: The fitted shape parameters n increase exponentially with downstream distance x. The three sets of filled markers correspond to three random realizations of the porous medium.

distributions $P(C)$ and $Q(C_1,C_2)$ will be obtained by first slicing the images of the fields into several rectangular regions, corresponding to increasing downstream distances x, and then calculating the pixelwise histograms in each of the regions [21].

III. MIXING PROPERTIES OF THE FLOW

A. Plume dispersion

The injected dye, transported by the vertical mean background flow, spreads in the transverse while it progresses in the medium. In order to characterize the spread of the plume of dye, we calculate its transverse width $\delta(x)$ at various downstream distances x as illustrated in Fig. 2(a). We define the transverse width $\delta(x)$ as the square root of the concentration-weighted variance of the transverse dispersion distance assuming radial symmetry of the dispersive plume. As seen in Fig. 3(b), the variance $\delta^2(x)$ scales linearly with the downstream distance x or, equivalently, with the time $t = x/u$ spent in the medium as

$$\delta(t)^2 = s_0^2 + 4D_\perp\, t \tag{1}$$

$$\text{with} \quad D_\perp \approx \frac{1}{20}\, u\, d, \tag{2}$$

a transverse dispersion coefficient $D_\perp$ which is consistent with known facts in the geometrical-disorder-induced dispersion regime at large Péclet number in porous media [11,12]. Note that, as seen on Fig. 3(b), the shape of the plume is invariant to the flow velocity, justifying the linearity $D_\perp \sim u$ of Eq. (2).

B. Growing sheets and necessary overlaps

The dispersion relation (1) gives the extent of the domain in which a kinematic activity at the smaller scale of the pores between the spheres distorts material surfaces. Because of the nonslip condition at the surface of the spheres constitutive of the porous medium, material elements are stretched by velocity gradients at the pore size and reoriented at random in the pore network at their passage frequency u/d. Thus, the injected stream soon resolves into a convoluted sheet, stretching and folding in the dispersion volume. We illustrate quantitatively the nature of the phenomenon by discussing the corrugation mechanism of a material line [22], the generalization to surfaces being straightforward.

1. Flow kinematics and material lines growth

We consider a blob of initial size s_0 and call $N(r,t)$ the number of segments of length r needed to cover its contour at time t. The current length of the contour, measured at scale r is thus $L(r,t) = rN(r,t)$. Between two consecutive instants of time, conservation of the number of segments stretched by the base flow writes $N(r + \Delta r, t + \Delta t) = N(r,t)$ and is equivalent to a Liouville equation

$$\frac{\partial N}{\partial t} + \left\langle \frac{\Delta r}{\Delta t} \right\rangle \frac{\partial N}{\partial r} = 0, \tag{3}$$

on ensemble average. Central to the dynamics of $N(r,t)$ is thus the r dependence of the separation (or pair dispersion) velocity $\langle \Delta r/\Delta t \rangle$ between two material points separated by r. A generic expression suitable for porous media is

$$\left\langle \frac{\Delta r}{\Delta t} \right\rangle = u(1 - e^{-r/d}) \tag{4}$$

interpolating, through a continuous crossover, between a linear shear regime $\langle \Delta r/\Delta t \rangle \sim \gamma r$ for $r/d \ll 1$ at the pore size (we call $\gamma \sim u/d$ the stretching rate) and a regime at larger scale for $r \gg d$ where the velocity difference between two points is typically given by u, independent of r. Of course, the velocity u, taken here as a representative mean velocity through the pores, is affected by random fluctuations, hence giving rise to the dispersion law in (1), as is well known (see, e.g., Refs. [1,10] and [23] for a similar formulation in turbulent flows involving a velocity rapidly fluctuating but with a permanent spatial structure).

Noticing that $d \ln(e^z - 1)/d z = 1/(1 - e^{-z})$ and following a procedure explained in Ref. [24], we obtain that for an initially smooth contour

$$N(r, t = 0) = \frac{s_0}{r}, \tag{5}$$

we have for any posterior time t

$$N(r,t) = \frac{s_0}{d}\{\ln[1 + e^{-\gamma t}(e^{r/d} - 1)]\}^{-1}. \tag{6}$$

The net blob contour length

$$L(t) = \lim_{r \to 0}\{rN(r,t)\} = s_0 e^{\gamma t} \tag{7}$$

increases exponentially in time at rate γ, reflecting the multiplicative nature of lengths stretching due to the ever-renewed reorientations, stagnation point splittings, and sustained stretch as the line elements pass through one pore to the next ones [3,25]. In this respect, advection through a porous medium is similar to what a turbulent flow would produce to the blob [22,26]. In synthetic porous media [2], the length $L(t)$ is better fitted with power laws as a function of the penetration depth in the medium, with an apparent exponent increasing with the disorder. It is likely that these power laws are broad transients toward the intrinsic, ultimate exponential regime in this problem where

the characteristic time γ^{-1} enforces the rescaling of time, even if it may take many γ^{-1} for the elongated line growth to reach it. This point is, nevertheless, still under debate.

The net blob length $L(t)$ is fundamentally different from the end-to-end dispersion distance $\delta(t)$, and the kinematic construction leading to (6) also explains why the line corrugates as it expands. It is *fractal* with a dimension $-d\ln N(r,t)/d\ln r$ whose scale dependence reflects the underlying stirring law (4), and it increases in time in an intermediate range of scales around d; both facts were observed earlier in related contexts [21,27]. Here, (6) predicts that the line will be space filling with a fractal dimension of 2 (for a line on the plane) at

$$\gamma t \approx 2.4, \quad \text{for} \quad r/d \approx 3. \tag{8}$$

These facts have two important consequences regarding the way molecular mixing proceeds in the medium, which we describe now.

2. *Mixing time and Batchelor scale*

We have just shown how a scale-dependent kinematic construction explains the net exponential growth of a blob contour length (equivalently, of its surface) and that the resulting expanding sheet will also be corrugated. A sheet expanding in area has, in an incompressible flow, a transverse with $s(t)$ which decays in time, and if the area growth rate is γ, one has $s(t) = s_0 e^{-\gamma t}$. Sheet thinning, and consequently concentration gradient steepening at the sheet surface, compete with diffusive broadening. The two effects balance at the mixing time t_s given by

$$t_s = \frac{1}{2\gamma}\ln \mathrm{Pe}, \quad \text{with} \quad \mathrm{Pe} = \frac{\gamma s_0^2}{D}, \tag{9}$$

where Pe is the blob Péclet number. From that time on, the sheet has reached its equilibrium thickness $s(t_s) = \sqrt{D/\gamma}$, known as the Batchelor scale [28], and as the sheet continues growing exponentially in area, and therefore in volume, its concentration in scalar decays exponentially quickly, like $e^{-\gamma t}$, by mass conservation.

To the mixing time corresponds a mixing distance $x_s = u\,t_s$ in the medium. With a dimensional estimate $\gamma = u/d \approx 0.5\ s^{-1}$ in the present experiments, we have $\mathrm{Pe} \approx 2\times 10^3$, $\sqrt{D/\gamma} \approx 45\ \mu$m, and $x_s \approx 3.8\,d$. It takes indeed roughly a depth corresponding to 3–4 sphere diameters for the concentration of the injected dye to start decaying [Fig. 1(c)]. This distance is also of the same order of magnitude as the distance for corrugations to be space filling that is anticipated in Eq. (8): At the same time the sheet mixes in the diluting flow, it also overlaps with itself.

3. *Overlaps enforced by confinement*

As it progresses through the medium, an element of sheet, expanding in area and volume, remains, however, confined inside the volume defined by its end-to-end dispersion. This is why, as explained in Sec. III B 1, the sheet has to overlap on itself. Consider an element of volume, say, $s_0^2 u\Delta t$ released by the source, at velocity u and concentration unity during the time interval Δt. This element will be spread out in a embedding dispersion volume $E(t)$ growing like

$$E(t) \sim u\Delta t \times \pi(\sqrt{D_\perp t})^2 \tag{10}$$

$$\sim u\Delta t\, d^2 \times \gamma t, \tag{11}$$

Because its area grows exponentially and its transverse thickness remains blocked at the Batchelor scale from t_s on, the volume $\Omega(t)$ of the sheet itself grows like

$$\Omega(t) \sim u\Delta t\, s_0^2\, e^{\gamma(t-t_s)} = u\Delta t\, s_0^2 \frac{e^{\gamma t}}{\sqrt{\mathrm{Pe}}}. \tag{12}$$

Obviously, since the sheet volume $\Omega(t)$ increases faster than its embedding environment volume $E(t)$, the sheet must overlap, and the mean number of overlaps $n(t)$ per sheet element is

$$n(t) = \frac{\Omega(t)}{E(t)} \underset{t \gg t_s}{\longrightarrow} e^{\gamma t}. \tag{13}$$

The overlaps, or aggregations, are mediated by molecular diffusion, by which the boundaries of nearby sheets, when they are brought to each other closer than the Batchelor scale, interpenetrate [2,29–32]. Since the concentration in an isolated sheet decays as $\theta \sim e^{-\gamma t}$, the concentration after n overlaps is $n\,\theta$ so that the average concentration of the mixture is

$$\langle C \rangle \sim \frac{\Omega(t)}{E(t)} \theta \sim \frac{s_0^2}{D_\perp t}, \tag{14}$$

or $\langle C \rangle \sim x^{-1}$, as seen in Fig. 3(a).

In chaotic [6] flows, turbulent flows [31], and porous media [2], aggregations occur at random, meaning that the sheet elements merge independently of the concentration C they carry. This maximal randomness interaction rule has a consequence on the way the mixture concentration distribution $P(C)$ is constructed, which, since it results from a random addition process in C space, has to be stable by self-convolution. Thus, it selects, after a few random additions, Γ distributions [31]

$$P(C) \overset{n \gg 1}{\longrightarrow} \Gamma_n(C), \tag{15}$$

$$\Gamma_n(c = C/\langle C \rangle) = \frac{n^n}{\Gamma(n)} c^{n-1} e^{-n\,c}, \tag{16}$$

where the shape parameter, or order, n is the aggregation count of merged elementary sheets in Eq. (13). In Fig. 3(c) are plotted the distributions $P(C)$ at various downstream locations x, obtained from an image of the field such as the one shown in Fig. 2(a). The distributions are not exactly Γ distributions because, if aggregations occur at random, they are more frequent at the center of the plume than at its edges. The divergence of $P(C)$ at small C is in particular due to this effect (see the discussion in Refs. [1,2]). We concentrate on the tail of the distribution, reflecting concentration levels mostly found at the center of the plume, a fact also known in turbulent flows [33,34], and from the fit with Eq. (16), we measure the parameter n, whose evolution as a function of the penetration depth x/d in the medium is shown in the inset of Fig. 3(c) for three independent realizations of the beads arrangement in the tank.

The corresponding exponential dependence is, remembering that $x = ut$, compatible with Eq. (13), with an apparent growth rate of the order of $\gamma = 0.2\,u/d$. This observation is interestingly compared with a prediction in Ref. [25], where the role of stagnation and separation points at the pore walls (beads in the present case) on the fluid elements deformation is analyzed. As the flow sequentially branches and merges around the spheres in the porous medium, the intensity of stretching depends of the angular reorientation between consecutive branching and merging events. In Ref. [25], the theoretical maximal stretching rate is $\gamma = \ln 2\,u/d$ for reorientations at 90°, while the configuration with random angular reorientation gives $\gamma = 0.12\,u/d$. Our result $\gamma = 0.2\,u/d$ is not far from it, indicating the extent of randomness of the flow.

Also, $n = 1$ is obtained for $x/d = 3.7$, very close to the mixing distance x_s expected from Sec. III B 2. Furthermore, from images like in Fig. 2(b), a visual inspection of the alternating stripes in the interbead space at various downstream locations gives qualitative but direct support for the interpretation of n as a sheet aggregation count.

These observations, linking flow kinematics and concentration content, support the random aggregation scenario for the construction of the mixture concentration distribution. Further proof is provided by examining the interaction rule of two subparts of the mixture.

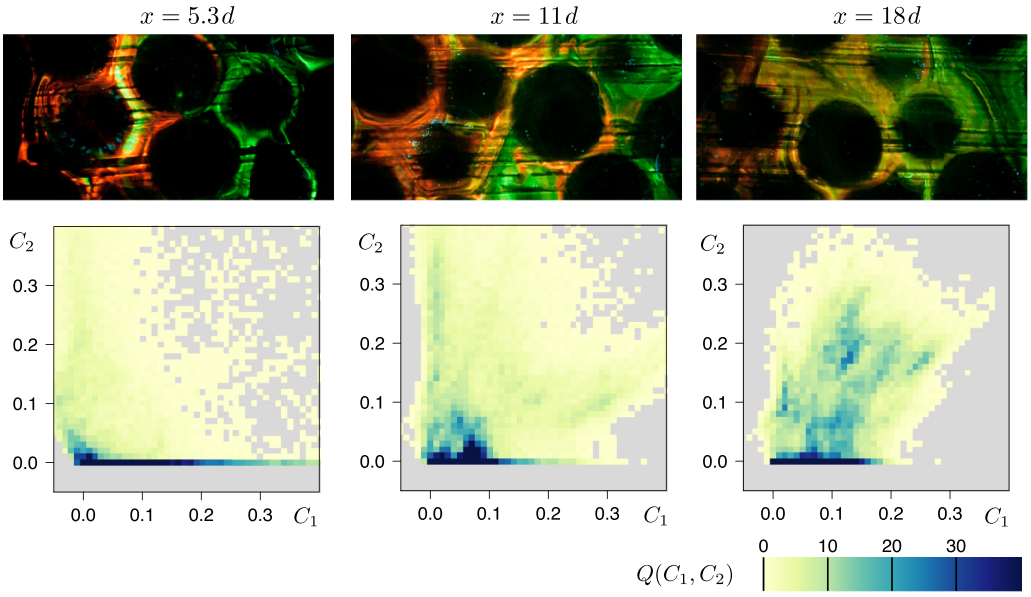

FIG. 4. Top row: three regions of the field at various downstream distances x, extracted from the image on Fig. 2(b) where the corresponding regions have been indicated by rectangular borders. Bottom row: the plots of joint distributions $Q(C_1,C_2)$ are calculated from the corresponding regions of the fields shown on top. The transition from initially anticorrelated fields C_1 and C_2 to interacting fields is qualitatively evident. Note that the two axes $C_1 = 0$ and $C_2 = 0$ are not symmetrical as a result of different absorbance and emission behavior of rhodamine and fluorescein.

C. Entangled fields

Using distinct dyes injected from the nearby separate sources as in Figs. 1(c) and 2(b), we now split the injection in two. The overall concentration field C is now decomposed in terms of its two subparts C_1 and C_2, thus allowing us to study how the two subfields have to be combined in order to restore the global field, and thus to assess the composition rule of the overall mixture [20].

1. Correlations and random additions

Scalar sheet elements aggregate diffusively, and as two elements from the distinct subparts of the field have once merged, they continue evolving as one. This inevitably leads to partially correlated stretching histories of the two subparts and, therefore, to a correlation of the concentration subfields. But since the count of random aggregations keeps increasing exponentially, the residual correlation progressively vanishes, giving rise ultimately to a purely random superposition of the fields.

From Fig. 2(b), we measure the joint distributions $Q(C_1,C_2)$, quantifying the probability of finding concentrations C_1 and C_2 of the two fields simultaneously present at a given point. In Fig. 4, three joint distributions Q at various downstream distances x/d are plotted along with the corresponding snapshots of the rectangular regions of the field used for calculating these distributions. Initially, close to the injection location, the concentration fields of the two dyes are fully segregated or anticorrelated. This is clearly seen from the leftmost plot of $Q(C_1,C_2)$ in Fig. 4, where most of the nonzero levels of Q are preferentially placed along the axes $C_1 = 0$ and $C_2 = 0$. At larger downstream distances x, these nonzero levels transition progressively toward the diagonal, as seen in the rightmost plot of Fig. 4, a sign of progressive loss of initial anticorrelation.

As recalled above Eq. (16), Γ distributions for $P(C)$ imply that the concentration field proceeds from random additions. Using a single dye, we have only indirectly verified the randomness by matching the measured concentration distributions with the predicted Γ's. However, with two

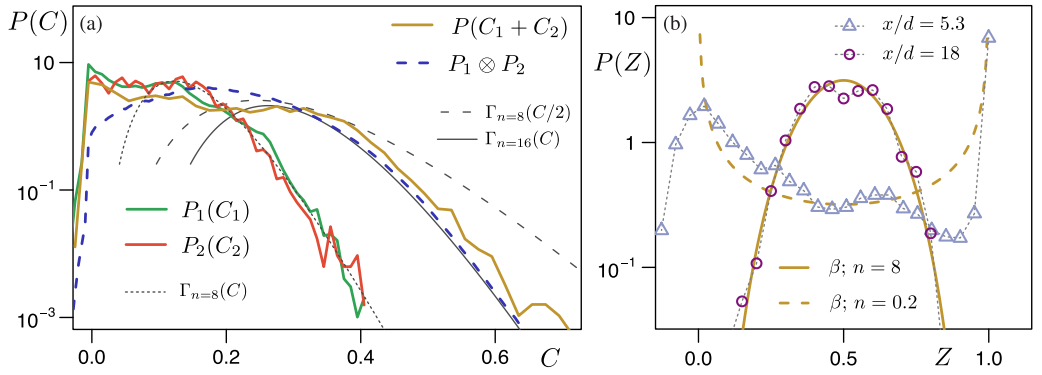

FIG. 5. (a) The three thick solid lines indicate the distributions of individual concentrations $P_1(C_1)$ and $P_2(C_2)$ and the total concentration $P(C = C_1 + C_2)$ extracted from the joint distribution $Q(C_1,C_2)$ at location $x = 18\,d$ shown on Fig. 4, right. The thick dashed line indicates the calculated convolution of $P_1(C_1)$ and $P_2(C_2)$. The thin dotted line is a weighted Γ distribution of shape parameter $n = 8$. The thin solid line is self-convolution of the thin dotted line and thus a weighted Γ distribution of shape parameter $n = 16$. For comparison, the thin dashed line indicates the distribution of the sum $C_1 + C_2$ in the case of two fully correlated Γ distributions. (b) The two lines with markers correspond to conditional distributions $P(Z|C)$ of the mixing ratio $Z = C_1/C$ confined to range $0.2 < C < 0.4$ that are calculated from two of the three joint distributions $Q(C_1,C_2)$ shown on Fig. 4. The thick solid line indicates a fitted β distribution [Eq. (23)] of shape parameter $n = 8$ matching well with the measured $P(Z)$ at the late stage of the mixture. The fully correlated case would result in Dirac δ in $Z = 0.5$. The thick dashed line indicates a β distribution of shape parameter less than unity $n < 1$ qualitatively matching the shape of measured $P(Z)$ at the segregated stage of the mixture.

distinct dyes, we can now directly check the applicability of the convolution scenario for which the total concentration field $C = C_1 + C_2$ must emerge from a random overlap of the two individual concentration fields C_1 and C_2. Thus, the overall distribution $P(C_1 + C_2)$ must be built as a convolution of the two individual distributions $P_1(C_1)$ and $P_2(C_2)$ as

$$P_1 \otimes P_2\,(C) = \int P_1(C_1)P_2(C - C_1)\,dC_1. \tag{17}$$

From the joint distribution $Q(C_1,C_2)$ measured at downstream distance $x = 18\,d$, we compute the individual distributions $P_1(C_1)$ and $P_2(C_2)$ as well as the overall distribution of the total concentration $P(C_1 + C_2)$ by, for instance,

$$P(C) = \int Q(C_1,C - C_1)dC_1 \quad \text{or,} \quad P_1(C_1) = \int Q(C_1,C_2)dC_2. \tag{18}$$

The three distributions are plotted with solid lines in Fig. 5(a). The thin dotted line is a Γ distribution of order $n = 8$, and the thick dashed line corresponds to the convolution calculated from the two measured individual distributions.

First, the distributions of each subfield are identical, because each field has, statistically, experienced the same stretching history from their nearby injection location to the downstream measurement location; both distributions are well fitted by a Γ distribution of order $n = 8$. Second, and more remarkable, the global distribution inferred from the convolution of the measured subfield distributions $P_1(C_1)$ and $P_1(C_1)$ matches very well the measured global distribution $P(C)$. This is a strong proof of the random nature of the aggregation process giving rise to C in the present porous medium: The neighboring subparts of the field which have been brought into contact and merged diffusively have experienced independent and uncorrelated stretching histories.

Note that if the two fields C_1 and C_2 were fully correlated, their superposition $C = C_1 + C_2 = 2C_1$ would be described by $P_1(C_1 = C/2)$, a limit which clearly does not represent the experiments [see the thin gray dashed line in Fig. 5(a)].

2. *Mixing ratio*

Another way of addressing further the nature of the correlation between the two sub-fields in the medium is to extract the one-dimensional conditional distribution $P(Z|C)$ of the mixing ratio

$$Z = \frac{C_1}{C_1 + C_2} \tag{19}$$

conditioned by a fixed total concentration $C = C_1 + C_2$. This quantity, whose interest is obvious if the distinct species injected are chemically reactive with a reaction rate dependent on the concentrations, is bounded between $Z = 0$ and $Z = 1$, these extremes corresponding to regions where only one of the two colors is present. The conditional distribution $P(Z|C)$ for C in a given range $C_{\text{low}} < C < C_{\text{high}}$ is obtained in the following way: first, a subpart of the joint distribution $Q(C_1,C_2)$ is extracted from the diagonal region $C_{\text{low}} < C_1 + C_2 < C_{\text{high}}$; then, the filtered subpart $Q_F(C_1,C_2)$ is mapped to the one-dimensional distribution of the mixing ratio Z as

$$P(Z|C) = \int Q_F\left(C_1, \frac{1-Z}{Z}C_1\right) dC_1. \tag{20}$$

Two distributions $P(Z|C)$ of the mixing ratio Z measured at two of the three downstream locations x of the plots of Q shown in Fig. 4 and conditioned by the total concentration in the range $0.2 < C < 0.4$ are plotted in Fig. 5(b). That range corresponds to the concentration levels found at the core of the plume, where the two fields interact substantially; small concentrations where the individual distributions $P(C)$ deviate from Γ distributions [Fig. 5(a)] are thus eliminated. Initially, the two fields are anticorrelated and segregated, as evidenced by the two peaks at $Z = 0$ and $Z = 1$. These peaks progressively leave place to a bell-shaped distribution around intermediate Z values, which is finally well represented by a β distribution when the two fields have overlapped at random.

The two pieces of information displayed in Fig. 5 are in fact redundant and are just two equivalent facets of the same reality, expressing the maximal randomness of the interaction rule between subparts of the mixture: Consider two individual distributions $P_1(C_1)$ and $P_2(C_2)$ of two independent variables C_1 and C_2. If the fields are entangled at random, then the joint distribution of the two fields is simply $Q(C_1,C_2) = P_1(C_1)P_2(C_2)$, while the joint distribution $F(C,Z)$ of the mixing ratio $Z = C_1/(C_1 + C_2)$ and of the total concentration $C = C_1 + C_2$ is

$$F(C,Z) = C\,P_1(CZ)P_2[C(1-Z)]. \tag{21}$$

When P_1 and P_2 are Γ distributed like $P_1(C_1) = C_1^{\alpha-1}e^{-C_1}/\,\Gamma(\alpha)$ and $P_2(C_2) = C_2^{\beta-1}e^{-C_2}/\,\Gamma(\beta)$, then

$$F(C,Z) = \Gamma_{\alpha+\beta}(C)B(Z;\alpha,\beta), \tag{22}$$

where

$$B(Z;\alpha,\beta) = \frac{\Gamma(\alpha+\beta)}{\Gamma(\alpha)\Gamma(\beta)}Z^{\alpha-1}(1-Z)^{\beta-1}, \tag{23}$$

is known [35] as the β distribution of shape parameters α and β. The joint distribution $F(C,Z)$ is a product of two independent distributions for C and Z.

A remarkable corollary of this result in the context of our two Γ distributed subfields of order n is the fact that the conditional distribution $P(Z|C) \equiv P(Z)$ of the mixing ration Z is independent of the conditional concentration C and takes the form of a β distribution of order $\alpha = \beta = n$. Also, C is Γ distributed with order $\alpha + \beta = 2n$. This is apparent in Fig. 5(b), where the measured distribution $P(Z)$ is well fitted by a β distribution with parameter $n = 8$ when the original subfields

are Γ distributed with the same shape parameter [see the dotted line in Fig. 5(a)]. This match further validates the conjecture that passively transported scalar mixtures in porous media mix according to a fully random interaction rule.

IV. CONCLUSION

We have shown that a stream of scalar injected into a porous medium soon resolves into an expanding stretched sheet as it progresses inside the medium. The convoluted sheet, which is the support of the concentration field, grows in volume faster than the dispersion volume in which it is embedded, forcing overlaps of the sheet with itself. These diffusive overlaps, or aggregations, whose number increases exponentially as a function of the age of the mixture in the medium, drive it toward its concentration content uniformity. Overlaps occur at random, as suggested by the shape, and rate of deformation of the concentration distribution of the mixture, which is constructed by self-convolution. The very existence of that particular route toward uniformity was further confirmed by splitting the mixture into two distinct color fields, showing that any residual correlation of the initially merged dyes is progressively hidden by the ever-increasing number of aggregations, leading to an effective fully random interaction rule of the two distinct subfields.

ACKNOWLEDGMENT

The French "Agence Nationale de la Recherche" is acknowledged for funding of the ANR-DFG TurbMix (ANR-14-CE35-0031-01).

[1] E. Villermaux, Mixing in porous media, C. R. Mecan. **340**, 933 (2012).
[2] T. Le Borgne, M. Dentz, and E. Villermaux, The lamellar description of mixing in porous media, J. Fluid Mech. **770**, 458 (2015).
[3] D. R. Lester, M. Dentz, and T. Le Borgne, Chaotic mixing in a three-dimensional porous media, J. Fluid Mech. **803**, 144 (2016).
[4] C. Simonnet and A. Groisman, Chaotic Mixing in a Steady Flow in a Microchannel, Phys. Rev. Lett. **94**, 134501 (2005).
[5] P. Carrière, On a three-dimensional implementation of the baker's transformation, Phys. Fluids **19**, 118110 (2007).
[6] E. Villermaux, A. D. Stroock, and H. A. Stone, Bridging kinematics and concentration content in a chaotic micromixer, Phys. Rev. E **77**, 015301 (2008).
[7] M. Dentz, T. Le Borgne, A. Englert, and B. Bijeljic, Mixing, spreading, and reaction in heterogeneous media: A brief review, J. Contam. Hydrol. **120**, 1 (2011).
[8] P. V. Danckwerts, Continuous flow systems, Chem. Eng. Sci. **2**, 1 (1953).
[9] J. M. Coulson, J. F. Richardson, J. R. Backhurst, and J. H. Harker, *Chemical Engineering*, 5th ed. (Butterworth-Heinemann, Oxford, UK, 2002), Vol. 2.
[10] J. Bear, *Dynamics of Fluids in Porous Media* (Elsevier, New York, 1972).
[11] J. J. Fried and M. Combarnous, Dispersion in porous media, Adv. Hydrosci. **7**, 169 (1971).
[12] J. M. P. Q. Delgado, Longitudinal and transverse dispersion in porous media, Chem. Eng. Res. Des. **85**, 1245 (2007).
[13] P. G. de Gennes, Hydrodynamic dispersion in unsaturated porous media, J. Fluid Mech. **136**, 189 (1983).
[14] J. P. Bouchaud and A. Georges, A simple model for hydrodynamic dispersion, C. R. Acad. Sci. Paris **307**, 1431 (1988).
[15] B. Bijeljic, P. Mostaghimi, and M. J. Blunt, Signature of Non-Fickian Solute Transport in Complex Heterogeneous Porous Media, Phys. Rev. Lett. **107**, 204502 (2011).

[16] U. M. Scheven, D. Verganelakis, R. Harris, M. L. Johns, and L. F. Gladden, Quantitative nuclear magnetic resonance measurements of preasymptotic dispersion in flow through porous media, Phys. Fluids **17**, 117107 (2005).
[17] M. Stöhr, K. Roth, and B. Jähne, Measurement of 3d pore-scale flow in index-matched porous media, Exp. Fluids **35**, 159 (2003).
[18] http://autourdelafleur.fr/
[19] M. Souzy, H. Lhuissier, E. Villermaux, and B. Metzger, Stretching and mixing in sheared particulate suspensions, J. Fluid Mech. **812**, 611 (2017).
[20] J. Duplat, A. Jouary, and E. Villermaux, Entanglement Rules for Random Mixtures, Phys. Rev. Lett. **105**, 034504 (2010).
[21] E. Villermaux and C. Innocenti, On the geometry of turbulent mixing, J. Fluid Mech. **393**, 123 (1999).
[22] E. Villermaux and Y. Gagne, Line Dispersion in Homogeneous Turbulence: Stretching, Fractal Dimensions and Micromixing, Phys. Rev. Lett. **73**, 252 (1994).
[23] R. H. Kraichnan, Anomalous Scaling of a Randomly Advected Passive Scalar, Phys. Rev. Lett. **72**, 1016 (1994).
[24] E. Villermaux, On dissipation in stirred mixtures, Adv. Appl. Mech. **45**, 91 (2012).
[25] D. R. Lester, G. Metcalfe, and M. G. Trefry, Is Chaotic Advection Inherent to Porous Media Flow? Phys. Rev. Lett. **111**, 174101 (2013).
[26] S. Kida and S. Goto, Line statistics: Stretching rate of passive lines in turbulence, Phys. Fluids **14**, 352 (2002).
[27] H. J. Catrakis and P. E. Dimotakis, Mixing in turbulent jets: Scalar measures and isosurface geometry, J. Fluid Mech. **317**, 369 (1996).
[28] G. K. Batchelor, Small-scale variation of convected quantities like temperature in turbulent fluid, part 1: General discussion and the case of small conductivity, J. Fluid Mech. **5**, 113 (1959).
[29] E. Villermaux and J. Duplat, Mixing as an Aggregation Process, Phys. Rev. Lett. **91**, 184501 (2003).
[30] S. Goto and S. Kida, Reynolds-number dependence of line and surface stretching in turbulence: Folding effects, J. Fluid Mech. **586**, 59 (2007).
[31] J. Duplat and E. Villermaux, Mixing by random stirring in confined mixtures, J. Fluid Mech. **617**, 51 (2008).
[32] T. Le Borgne, P. D. Huck, M. Dentz, and E. Villermaux, Scalar gradients in stirred mixtures and the deconstruction of random fields, J. Fluid Mech. **812**, 578 (2017).
[33] Z. Warhaft, The interference of thermal fields from line sources in grid turbulence, J. Fluid Mech. **144**, 363 (1984).
[34] M. A. Soltys and J. P. Crimaldi, Joint probabilities and mixing of isolated scalars emitted from parallel jets, J. Fluid Mech. **769**, 130 (2015).
[35] W. Feller, *An Introduction to Probability Theory and Its Applications* (John Wiley and Sons, New York, 1970).